Original Research

Direct Comparison of Myocardial Perfusion Cardiovascular Magnetic Resonance Sequences with Parallel Acquisition

Jonathan C. Lyne, MRCP,[1] Peter D. Gatehouse, PhD,[1] Ravi G. Assomull, MRCP,[1] Gillian C. Smith, MSc,[1] Peter Kellman, PhD,[2] David N. Firmin, PhD,[1] and Dudley J. Pennell, FRCP, FESC, FACC[1]*

Purpose: To directly compare the three main myocardial perfusion cardiovascular magnetic resonance (CMR) sequences incorporating parallel acquisition methods.

Materials and Methods: In 15 subjects (12 men, 57 ± 15.7 years) referred for diagnostic coronary angiography, we acquired first-pass perfusion images (0.1 mmol/kg gadolinium-DTPA) at rest and during adenosine (140 μg/kg/min) on three separate occasions using three sequences incorporating parallel acquisition methods and approximately equivalent spatiotemporal resolution: hybrid echo planar imaging (hEPI), steady-state free precession (SSFP), and gradient echo imaging (GRE). We calculated the contrast-to-noise ratio (CNR) of each scan and blinded observers scored the presence and severity of artifacts (1, worst to 4, best), diagnostic confidence (0, low to 2, high), transmurality, area, and epicardial vessel territory of perfusion defects.

Results: CNR was greatest with SSFP and least with hEPI (13.15 vs 7.85 $P < 0.001$). The most artifacts were recorded with SSFP and least with hEPI (2.00 vs 3.03 $P < 0.001$). Observers were significantly more confident in reporting hEPI images (1.6 hEPI vs 0.9 SSFP, $P < 0.001$). Results for GRE were intermediate for all assessments.

Conclusion: The hEPI sequence scored best for diagnostic performance despite the SSFP sequence having greater CNR. This trial favors hEPI for clinical myocardial perfusion CMR and suggests CNR should not be the sole criterion used to gauge the best candidate sequence.

Key Words: MRI; myocardial perfusion; first-pass; gadolinium contrast agent
J. Magn. Reson. Imaging 2007;26:1444–1451.

CARDIOVASCULAR MAGNETIC RESONANCE (CMR) can assess myocardial perfusion (1) and myocardial infarction (2,3) at higher in-plane spatial resolution than existing techniques, potentially improving diagnostic accuracy without ionizing radiation. However, the optimal sequence for myocardial perfusion CMR has not been determined. Most studies have used either a fast low-angle single-shot gradient-echo sequence (GRE) (4–7), single-shot echo-planar imaging (8,9), or a hybrid EPI sequence (hEPI) (10,11). More recently, a steady-state free precession sequence (SSFP) technique has been used (12,13). The GRE sequence has a short time between RF pulses with spoiling of the transverse magnetization requiring a low flip angle, thus limiting signal and contrast-to-noise ratios (CNRs). The hEPI sequence has potential advantages as it collects multiple data lines after each RF pulse. The increased repetition time permits higher flip angles for potentially higher signal and CNR, while fast data acquisition permits comprehensive myocardial coverage with good spatiotemporal resolution, potentially reducing artifacts. The SSFP sequence reuses transverse magnetization, resulting in improved signal and CNR compared with GRE (14), although it may be more prone to artifacts.

A further refinement of the perfusion sequences would be sequence acceleration, permitting improved spatiotemporal resolution and/or improved myocardial coverage (15,16). This may improve image quality by reducing motion artifact within a shorter image acquisition duration, although any such improvement might be at the cost of a lower signal-to-noise ratio (SNR) and artifacts (17,18). Two parallel acquisition methods (PAM) are currently in routine clinical use: generalized autocalibrating partially parallel acquisition (GRAPPA) (19) and sensitivity encoding (17,20). Acceleration of imaging is achieved by reducing the number of acquired phase-encoding lines. Both methods use data from the perfusion scan acquisition to estimate spatial coil sensitivity. While GRAPPA samples these additional central lines reducing the effective acceleration rate, inclusion of this data within the center of *k*-space compensates for some of the predicted signal loss. Adaptive sensitiv-

[1]Cardiovascular Magnetic Resonance Unit, Royal Brompton Hospital, London, UK.
[2]Laboratory of Cardiac Energetics, NHLBI, National Institutes of Health, DHHS, Bethesda, Maryland.
*Address reprint requests to: Prof. D.J. Pennell, CMR Unit, Royal Brompton Hospital, Sydney St., London SW3 6NP, UK.
E-mail: d.pennell@rbht.nhs.uk
Received September 30, 2006; Accepted August 15, 2007.
DOI 10.1002/jmri.21167
Published online 26 October 2007 in Wiley InterScience (www.interscience.wiley.com).

ity encoding incorporating temporal filtering (TSENSE) combines temporally interleaved *k*-space lines to generate coil sensitivity maps directly from image data (18), and therefore there is no oversampling within central *k*-space. There are two potential advantages of TSENSE over GRAPPA: faster acquisition by deriving coil sensitivity maps from routinely acquired data and more robust coil sensitivity estimation by temporal filtering of the data. The temporal resolution of the coil sensitivity map is lowered by averaging data across multiple frames (usually 8) but image data used for reconstruction are not shared or interpolated.

We directly compared the three main myocardial perfusion CMR sequences incorporating PAM. We hypothesized that the perfusion sequences would perform differently in terms of artifacts, diagnostic accuracy, and CNR.

MATERIALS AND METHODS

We compared GRE, hEPI, and SSFP perfusion sequences utilizing a PAM and assessed the relative CNR, observer diagnostic confidence, size of inducible perfusion defects, and presence of artifact. We studied 15 patients (12 men, mean age 57 ± 15.7 years) undergoing x-ray coronary angiography. Angiographic data were recorded by quantitative coronary angiography (QCA) (Medcon, Whippany, NJ). The three major coronary arteries and their first-order branches >2 mm diameter were assessed. Five patients had known previous myocardial infarction. Three patients had two vessel disease, and five had triple vessel disease. Seven patients had unobstructed coronary arteries with either minor atheroma (three) or smooth epicardial vessels (four). Three patients had previously undergone revascularization: two percutaneously, one coronary artery bypass surgery. Patients with atrial fibrillation, contraindications to CMR or adenosine were excluded. All 15 subjects underwent imaging with all three sequences, each performed on a separate visit. Sequence acquisition order was randomized. Studies were performed on a 1.5T MR scanner (Siemens Sonata, Erlangen, Germany) with a 12-element phased array cardiac coil (Siemens). The study was approved by the local ethics committee and each subject gave written informed consent. Subjects abstained from caffeine products for 24 hours prior to each study.

Parameters for the three pulse sequences are displayed in Table 1. The pulse sequences were used as provided by the manufacturer (software version MR2002B 4VA21A). All three sequences were applied with the following parameters in common. A rectangular field of view (FOV) was used. Read FOV 34–40 cm; phase FOV 75% of the read FOV; base matrix 128 × 96; pixel size range 2.7 × 2.7 mm at 34 cm FOV, increasing to 3.1 × 3.1 mm at 40 cm FOV. The phase FOV was fixed at 75% of read FOV to ensure that the T1-weighting did not vary. The saturation preparation time for each sequence varied slightly but temporal resolution was similar for all three sequences (Table 1). Bandwidth was optimized for each sequence (Table 1) such that three 8-mm-thick short-axis slices could be acquired within 550 msec, appropriate for clinical perfusion imaging. All three sequences used a nonselective square saturation pulse of 90°. All three sequences also used full ky-coverage. No filtering was applied to the reconstruction of any sequence.

Table 1
Pulse sequence parameters

	Pulse Sequence		
	hEPI	SSFP	GRE
TR (ms)	5.8	2.2	2.4
TE (ms)	1.22	1.0	1.2
Read FOV (cm)	34-40	34-40	34-40
Phase FOV (cm)	25.5-30	25.5-30	25.5-30
TD (ms)	74	33	6
Flip angle	30°	50°	12°
Time from saturation pulse to centre of K space (ms)	108	91	80
Image data acquisition time per slice (ms)	69	114	142
Total time per slice including saturation preparation (ms)	146	147	152
Bandwidth (Hz/pixel)	1860	1400	550
Parallel acquisition method	TSENSE	TSENSE	GRAPPA
Effective acceleration factor (R)	2	2	1.6

TR = pulse sequence repetition time. TE = Echo time. FOV = field of view. PAM = parallel acquisition method. TD = time delay following saturation pulse to the first imaging RF pulse, including fat saturation (18ms) for hEPI and SSFP.

The hEPI (11) sequence was an interleaved segmented-EPI sequence with RF spoiling, acquiring four gradient-echoes per RF pulse (EPI factor or echo-train-length 4). This sequence used a center out phase encode order such that the center of *k*-space was acquired on the first echo (11). Echo-time shifting was used to further reduce EPI ghosting due to fat or off-resonance by eliminating discontinuities in *k*-space caused by jumps in TE. No velocity compensation was used on the slice select axis nor on the first sampled echo. Fat saturation was used to reduce EPI ghosting due to fat (21). The TSENSE (18) acceleration rate was 2 (sliding average of 8 frames for coil sensitivity maps).

The SSFP sequence (13) allowed asymmetric echoes (22), used fat saturation, and a TSENSE (18) acceleration rate of 2 (sliding average of 8 frames for coil sensitivity maps). For steady-state stabilization, the SSFP used five dummy cycles with linear flip angle preparation (23) before it started to acquire data in the conventional top-down phase-encode order. (The frequency encode waveform had fast ramps, and a constant sampling gradient and ADC sampling rate was used, unlike Ref. 13.)

The GRE sequence (24) had no extra gradient spoiling beyond that of the residual frequency-encode and slice-select areas, presumably for maximum speed. The absence of phase-encode rewinding reduces the effectiveness of RF spoiling and may also cause striping patterns (25), but this artifact was not observed in vivo at the 12° flip-angle used. The GRE sequence was also initially implemented with TSENSE. However, artifacts were noted across the FOV of a crosshatched pattern

(checkerboard noise burst) because the nonselective saturation was initiating a stimulated echo artifact most apparent in the GRE-TSENSE sequence. Following identification of this artifact at an early stage we decided to acquire data with the GRAPPA (19) parallel imaging method, where this artifact was reduced by virtue of the slight change in timing due to additional central *k*-space lines acquired. The GRAPPA (19) acceleration factor was 2 (effective acceleration 1.6 when including 24 reference lines in central *k*-space).

Gadolinium-DTPA (Magnevist; Schering, Berlin, Germany) 0.1 mmol/kg of body weight was injected at 7 mL/s (Spectris; Medrad, Indianola, PA) via an 18-gauge cannula in the right arm followed with 15 mL normal saline at 7 mL/s. During each first-pass study patients held their breath for as long as comfortable at end-expiration. Rest imaging was performed at least 20 minutes after the stress study with adenosine (140 mcg/kg/min; Fujisawa Healthcare, Deerfield, IL). Adenosine was infused intravenously for 4 minutes via a 20-gauge cannula in the left arm. Heart rate was monitored continuously and blood pressure was measured preceding and 3 minutes following initiation of adenosine infusion. Three short-axis sections were acquired during each cardiac cycle over 50 consecutive cycles, permitting a 16-segment analysis. The only segment not imaged was the apical segment. Basal slice positioning avoided the left ventricular outflow tract; mean slice separation 160% (range 100%–200%) of slice thickness. The basal image was acquired first followed by mid then apical slices. Short-axis images obtained during the first visit were used to obtain short-axis images at repeat visits with identical slice separation, ensuring consistent imaging. All image analysis was performed offline using dedicated software (CMRtools; Cardiovascular Imaging Solutions, UK). All images were randomized and scorers blinded to the sequence used and patient details.

In the mid ventricular short-axis section a myocardial region of interest (ROI) was drawn in each wall (anterior, lateral, inferior, and septal), generating four ROIs for each study. Regions were drawn as large as possible but avoiding contamination from nearby tissues. ROI positions were manually adjusted to compensate for respiratory and cardiac motion. Study-to-study transfer of ROIs was possible, providing a consistent regional assessment. We were unable to correct for through-plane motion.

Signal and CNR measurements were based on background noise measured from perfusion images. In parallel imaging background noise may be highly variable across the FOV (17,26), therefore measurements were made in the vicinity of the myocardial ROIs. To avoid contaminating noise measurement with signal contribution, the noise standard deviation was measured during the precontrast period of low signal intensity and images further filtered to remove the signal. Noise was measured in the LV blood pool, providing a large ROI with relatively homogenous signal intensity. To suppress spatial inhomogeneity due to surface coil variation a high-pass spatial filter as well as temporal standard deviation (8 frames during precontrast) were used. The high-pass spatial filter had a calibrated scale factor providing accurate noise measurement, which compensated for the change in noise level due to filtering. This method which used a high-pass spatial filter and temporal standard deviation is a generalization of the method using simpler spatial differentiation to provide improved suppression of the blood pool signal and extraneous artifacts (27). The method was validated against a volunteer study that used prescan noise-based SNR scaled reconstruction (26). The prescan-based approach requires reconstruction from raw data that were not available for all the clinical studies. This method assumes minimal variation in the coil geometric factor (g) between sampled myocardium and blood pool within the selected slice. To calculate the CNR, precontrast mean (averaging 4 time frames) myocardial ROI signal intensity was subtracted from mean (averaging 4 time frames) myocardial ROI signal intensity at peak enhancement postcontrast. This was then divided by the noise value for each scan (28). The CNR of induced defects was not specifically assessed. Only stress images were analyzed; previous studies have not shown significant differences in CNR between rest and stress scans (29).

Two experienced blinded observers independently assessed the presence and degree of artifacts and assigned a diagnostic confidence score. Artifacts were only recorded by the observers if myocardial imaging was affected. These artifacts were usually a transient dark subendocardial band or rim arising from a mixture of Gibbs, susceptibility, and motion effects. This particular effect was separated from genuine defects subjectively, based on its correlation with the blood signal brightness and its tendency to occur also in the rest scan. Other effects were included in the artifact scoring such as parallel imaging N/2 artifact, if this obscured any myocardium. The presence and severity of artifacts was scored as: 1, severe artifact; 2, moderate; 3, mild; and 4, none.

The diagnostic confidence score reflected subjective observer confidence in the presence and severity of any perfusion defect, with a nondiagnostic scan scored 0, low diagnostic confidence 1, and high diagnostic confidence 2. Diagnostic confidence was reduced by any suspicion of subendocardial banding artifact, and there was some overlap between the artifact score and the diagnostic confidence score. Diagnostic confidence was also reduced by poor myocardial image quality, for example, low SNR or blurred subendocardial borders.

The number of myocardial segments, area and transmural extent of inducible perfusion defects were measured across all three short axis slices. For subsequent analysis of these parameters the average of measurements obtained by both observers was used. On a second occasion observers reviewed images together, blinded to the sequence used and the patients clinical status, recording epicardial territories consistent with the segments of hypoperfused myocardium (30). In cases of disagreement between the two observers, a consensus decision was reached.

Statistical analysis was performed using SPSS software (v. 10; SPSS, Chicago, IL). Segmental CNR values and observer scores were analyzed with a Friedman test (nonparametric analysis of variance). Post-hoc analysis

Table 2
Haemodynamic parameters

	Rest				Stress			
	hEPI	SSFP	GRE	p value	hEPI	SSFP	GRE	p value
SBP	126 ± 17	129 ± 14	124 ± 16	p = 0.64	129 ± 20	131 ± 17	134 ± 19	p = 0.88
DBP	83 ± 7	81 ± 8	77 ± 7	p = 0.25	78 ± 9	74 ± 9	76 ± 10	p = 0.19
HR	64 ± 8	63 ± 7	65 ± 5	p = 0.61	78 ± 7	79 ± 14	79 ± 11	p = 0.72

SBP = Systolic blood pressure. DBP = diastolic blood pressure. HR = heart rate.
Haemodynamic parameters recorded at rest and stress during scans with each pulse sequence. Figures are mean values ± standard deviation. P values were not significant for comparisons across the three sequences.

was with a paired Wilcoxon signed rank test. Hemodynamic parameters were compared using a Friedman test. In all cases a *P*-value less than 0.05 was taken to indicate statistical significance.

RESULTS

All 15 volunteers completed the study, undergoing imaging with all three sequences. The mean number of days to complete all three acquisitions was 38 (range 3–178, SD 37). In the 45 perfusion studies subjects were able to hold their breath until after the first pass of gadolinium through ventricular myocardium. There were no significant differences in the hemodynamic measurements between rest and stress scans for the three sequences (Table 2). QCA data alongside mean observer scores are presented in Table 3.

CNR Values

There was a significant difference in CNR between all three sequences (Fig. 1). The greatest CNR was with the SSFP sequence (hEPI 7.85; SSFP 13.16; GRE 10.85; $P < 0.001$).

Artifacts

There was a significant difference in artifact scoring between the three sequences (Fig. 2). Most artifacts were observed in the SSFP scans. The hEPI sequence had the fewest artifacts (hEPI 3.03; SSFP 2.00; GRE 2.50; $P < 0.001$). Several different types of artifacts were noted with all three pulse sequences. First, and most frequent, the transient dark subendocardial bands reported often in myocardial perfusion work. Second, those due to misgating of image acquisition from the ECG recording. Third, checkerboard artifacts, particularly in the GRE sequence, as described previously, probably due to stimulated echo formation. Fourth, half FOV artifacts, particularly noted with the TSENSE reconstruction algorithm, due to failure of the sensitivity reconstruction algorithm when the reconstructed FOV is smaller than the imaged object. This also occurred with rapid motion within the eight averaged frames used to generate the B1 coil sensitivity map. This most commonly occurred during rapid inspiration toward the end of the acquisition and was not propagated throughout the series by averaging only eight frames.

Diagnostic Confidence Scoring

There was a significant difference in the scoring of the sequences (Fig. 3). The hEPI sequence scored highest (hEPI 1.6; SSFP 0.9; GRE 1.2; $P < 0.001$).

Induced Perfusion Defects

In the 45 studies there were a total of 1440 scored segments. The two observers both recorded inducible perfusion defects in 19 studies (223 segments). The two observers were concordant in the total number of segments scored hypoperfused in three studies. Figure 4 illustrates a case of concordance of both scorers recording a hypoperfusion defect with all three sequences. In 23 studies (368 segments) the observers were in agreement on the absence of any hypoperfused segment. Of these studies, seven were SSFP, eight GRE, and eight hEPI. In only three studies (four segments) did one observer score the presence of a defect not recorded by the other; two were SSFP, the other GRE. The correlation coefficient for the total number of segments scored by each observer in each of the 45 studies was 0.93. In two patients hEPI recorded a defect not identified by the two other sequences (Fig. 5). Despite this there was no significant difference between the two observers in the planimetered area of the perfusion defect (hEPI $P = 0.59$, SSFP $P = 0.48$, GRE $P = 0.14$). There was no significant difference in the area recorded by the two observers between the three sequences (hEPI 522 mm^2; SSFP 506 mm^2; GRE 418 mm^2; $P = 0.51$). There was also no difference in the percentage transmural extent of the maximal perfusion defect recorded by the two observers across all three sequences ($P = 0.25$, $P = 0.42$), or between each sequence (hEPI 48% $P = 0.42$; SSFP 33% $P = 0.28$; GRE 38% $P = 0.67$).

Infarctions

In 15 studies (five subjects) where late gadolinium enhancement (LGE) confirmed the presence of infarction (104 segments) observers identified hypoperfused segments in 10 studies at stress (109 segments). Therefore, in the majority of studies the number of hypoperfused segments was greater or equal to the number of LGE segments. No hypoperfused segment was recorded with all three sequences in one subject, in another no hypoperfused segment was recorded in the GRE-GRAPPA and hEPI-TSENSE studies. In these cases there was a single segment of subendocardial LGE within the inferolateral wall and the anterior wall, re-

Table 3
Angiographic data recorded by quantitative coronary angiography

Patient	QCA	hEPI	GRE	SSFP
1	LAD and OM1 occluded SVG to LAD 88% SVG to Intermediate occluded RCA(D) 33%	LAD LCX 1043mm^2 A3.5	LAD LCX 1965mm^2 A3.5	LCX 1564mm^2 A2.5
2	LAD 26% LCX(D) 31% RCA 46%	None A1.5	None A2	None A2
3	LAD 86% LCX 97% RCA(D) 23%	LAD LCX 1434mm^2 A4	LAD 746mm^2 A2.5	LAD LCX 667mm^2 A3
4	Occluded LAD LCX (distal) 89% RCA(D) 94%	LAD RCA 978mm^2 A3.5	LAD RCA 1458mm^2 A3	LAD RCA 1680mm^2 A3.5
5	Occluded LAD LCX 31% (OM1 76%), Occluded RCA(D)	LAD RCA 641mm^2 A3.5	RCA 110mm^2 A1.5	None A2
6	LAD (distal) 91% LCX 88% RCA(D) 93%	LCX 770mm^2 A3.5	LCX 555mm^2 A2.5	LAD LCX 1030mm^2 A1.5
7	Normal	None A3	None A3	None A2
8	LAD 41%	None A3	None A3	None A2
9	Normal	None A2.5	None A1.5	None A1.5
10	Normal	None A3.5	None A2	LCX 213mm^2 A2
11	Normal	None A3.5	None A2.5	None A1
12	Occluded intermediate LCX 27% RCA(D) 44%	LCX 1440mm^2 A3	None A2	None A1
13	LAD 31%	None A2.5	None A3	LCX 885mm^2 A3.5
14	Normal	None A2.5	None A0.5	None A1.5
15	LAD 77% LCX 98% Occluded RCA(D)	LCX RCA 1537mm^2 A3.5	LCX RCA 1443mm^2 A3.5	RCA 1222mm^2 A2

QCA = quantitative coronary angiography. LAD = left anterior descending artery. LCX = left circumflex artery. OM1 = first obtuse marginal artery. RCA = right coronary artery. SVG = Saphenous vein graft. The dominant inferior territory vessel, either the LCX or the RCA, is denoted by (D). For each of the sequences the epicardial vessel recorded by the observers, mean defect area (mm^2) and artifact scores (A) are also shown. Note patients 10 and 13 with defects recorded in the LCX territory in the presence of angiographically unobstructed epicardial coronary arteries, also patient 12 with only the hEPI sequence documenting a perfusion defect, although angiographically the occluded vessel was the intermediate artery.

spectively. In total, 17 LGE segments were not matched with a perfusion defect within the exact same segment and this occurred across all three sequences.

DISCUSSION

This study is the first direct comparison of the three main perfusion sequences utilizing PAM. Sequence acceleration resulted in the ability to acquire three short axis slices in all subjects at stress with all three sequences, such that the comparison is suitable for clinical ventricular sampling. This study is unusual because we performed each of the three sequences in every patient, which enhances the identification of intersequence differences.

The appearance of dark subendocardial artifacts, most apparent at the highest concentrations of gadolinium within the left ventricle, is a well-established weakness of CMR first-pass perfusion. Such subendocardial banding artifacts may be falsely interpreted as perfusion defects. Previous work has shown that car-

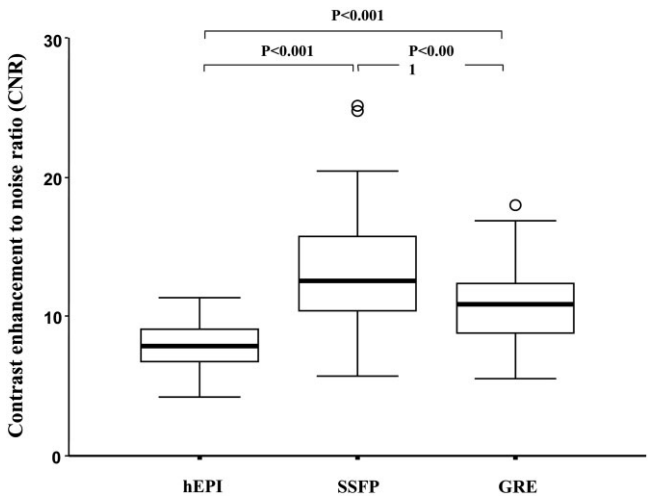

Figure 1. Boxplot of contrast enhancement to noise ratios for each sequence. The SSFP sequence had the highest CNR. Outliers are excluded from the boxplots for display but are included in the formal statistical analysis.

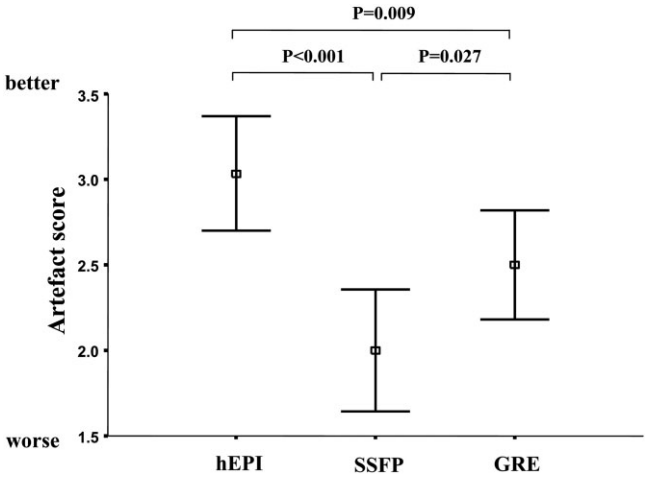

Figure 2. Observer artifact scoring for each of the three sequences displaying the mean value (bar and box) and 95% confidence intervals. A lower score represents more artifact. There was a significant difference between the sequences, with the hEPI sequence having fewer artifacts compared to both the SSFP and GRE sequences.

diac motion during image acquisition (31) and spatial resolution (32) may have a significant effect on the appearance of artifacts. Previous authors suggest that the prevalence of banding artifacts with SSFP is related to its greater inherent CNR in comparison to the other sequences (33). In this study SSFP had the greatest CNR, but also the most artifacts. The speed of data acquisition by the sequences appeared a good correlate, with the lower number and severity of artifacts seen with hEPI. The shorter acquisition duration of hEPI resulted in less cardiac motion during acquisition and therefore less blurring of both the image and induced perfusion defect, potentially increasing diagnostic confidence. This suggests that any perfusion sequence with a PAM incorporated should be less susceptible to

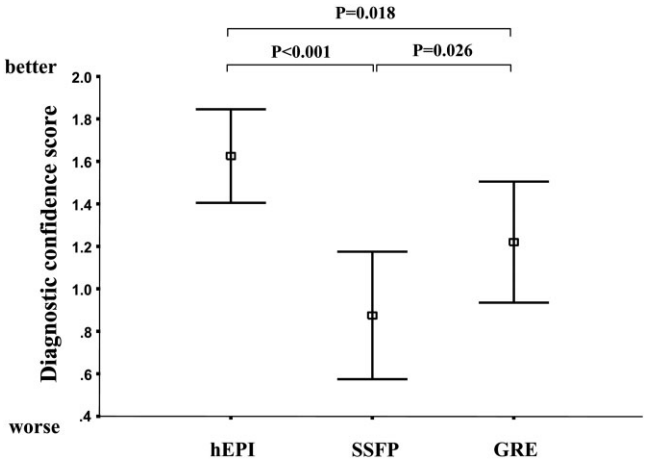

Figure 3. Observer scoring of diagnostic confidence displaying the mean value (bar and box) and 95% confidence intervals. A higher score represents a greater diagnostic confidence. There was a significantly higher confidence with the hEPI sequence compared to both the SSFP and GRE sequences.

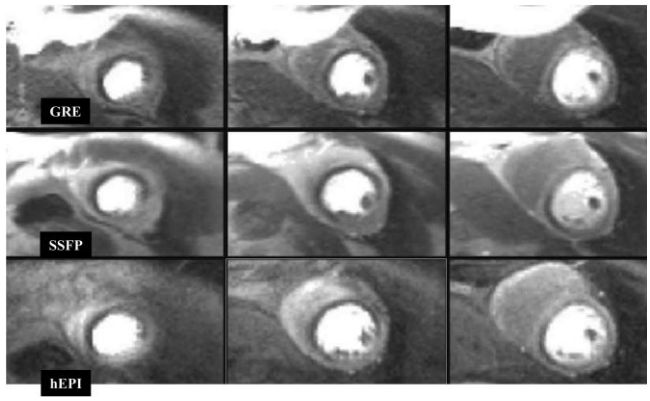

Figure 4. Concordant clinical findings between the three perfusion sequences. Images from the **(a)** GRE-GRAPPA, **(b)** SSFP-TSENSE, and **(c)** hEPI-TSENSE sequences in a patient with significant two-vessel disease (left anterior descending and right coronary artery). A severe perfusion defect is seen in the anterior, inferior, and septal walls at all three slice levels which is concordant for all sequences.

motion artifacts than an unaccelerated counterpart. However, parallel imaging reduces signal and CNR, with potential for artifacts due to the necessary reconstruction algorithms. These factors must be balanced against the probable reduction of dark rim artifacts seen with higher spatial resolutions permitted by a reduced acquisition time (32).

In this study hEPI-TSENSE and GRE-GRAPPA had a lower CNR than SSFP-TSENSE, which is consistent with the findings of Fenchel et al (12) and Schreiber et al (13), who also reported a higher SNR and CNR with an SSFP compared to a GRE perfusion sequence. The discrepancy of these findings with those of Elkington et al (29), who found superior CNR with hEPI compared to a GRE perfusion sequence, is likely due to the higher flip angle in the GRE sequence of this study. A significant difference in CNR between hEPI-TSENSE and GRE-GRAPPA is surprising, given the sequence param-

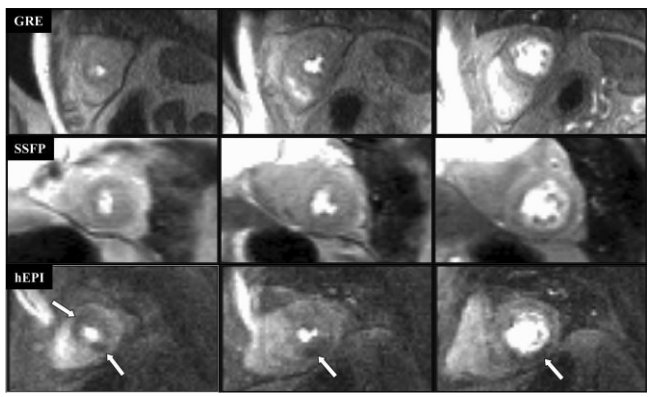

Figure 5. Discordant clinical findings between the three perfusion sequences. Images from the (a) GRE-GRAPPA, (b) SSFP-TSENSE, and (c) hEPI-TSENSE sequences in a patient with significant two-vessel disease. Note the relative contrast and clarity of the inducible perfusion defects in the hEPI-TSENSE image. This was not so readily identified by the other sequences.

eters used in this study. This probably results from differences in the PAM used: of 24 reference lines in the GRAPPA reconstruction, 12 were extra lines in addition to the 40 lines normally acquired; therefore, in total, 52 lines were used in image formation. It would be reasonable to surmise that the GRAPPA technique would have resulted in a relatively lower reduction in CNR and SNR than TSENSE, primarily due to the acquisition of these extra central *k*-space lines. Furthermore, the longer acquisition duration to sample these extra lines may explain some of the reduction in diagnostic performance with this sequence.

In this study the acceleration factor was similar across the three sequences. Future studies may utilize the inherently greater SNR with SSFP to permit greater acceleration factors with potentially fewer motion artifacts, increased myocardial coverage, and/or in-plane spatial resolution. The higher standard deviation for the SSFP CNR values in this study is unexplained but consistent with the findings of Fenchel et al (12), who proposed that this may be related to increased sensitivity of SSFP to inhomogeneous coil signal or higher inter- or intraslice variability of perfusion parameters.

There are previous data comparing myocardial perfusion sequences. Comparison of hEPI and GRE, showed comparable artifact and ischemia scores for hEPI (29). However, many studies have not necessarily had a suitable clinical dimension being limited by using doped phantoms, not comparing sequences in the same patients, performing only rest perfusion studies, or not systematically assessing the presence and severity of artifacts (33,34). In our study, hEPI scoring the least artifacts and the highest diagnostic confidence is consistent with the findings of Muhling et al (35), who demonstrated that interobserver agreement as well as sensitivity to perfusion defects is related to both image quality and SNR. In this study, a technical sequence comparison, we could not confirm that hEPI was associated with significantly improved diagnostic clinical performance because the very small sample size (15 patients) was insufficient for showing diagnostic differences. However, the sequence with the lowest number of artifacts and highest observer confidence (ie, hEPI) would be expected to have a clinical diagnostic advantage. Although the observers were blinded, we could not prevent them from estimating what sequence was used for each image from its appearance, so the possibility of subconscious bias cannot be excluded.

This study demonstrates that all three sequences with parallel imaging are capable of providing reasonable quality perfusion images with a spatiotemporal resolution of ≈160 msec per image at ≈3 mm in-plane resolution. Comprehensive myocardial coverage is critically important, as it is likely to determine sensitivity to the detection of coronary artery disease. Although a greater number of short axis slices are acquired by some centers, three slices has been considered by many as sufficient, ensuring myocardial coverage includes 16 of the 17 myocardial segments (30). There was sufficient time within the RR interval at stress in many cases, particularly with hEPI, to have acquired at least one long axis image to cover the apex. This is likely to be useful in the clinical utility of this imaging modality, improving not only diagnostic sensitivity but also diagnostic confidence.

In conclusion, the results show that although CNR was lowest for hEPI, these images were nonetheless scored with the highest diagnostic confidence and fewest artifacts. This favors the use of hEPI clinically, despite its technically inferior SNR performance.

REFERENCES

1. Schwitter J, Nanz D, Kneifel S, et al. Assessment of myocardial perfusion in coronary artery disease by magnetic resonance: a comparison with positron emission tomography and coronary angiography. Circulation 2001;103:2230–2235.
2. Kim RJ, Wu E, Rafael A, et al. The use of contrast-enhanced magnetic resonance imaging to identify reversible myocardial dysfunction. N Engl J Med 2000;343:1445–1453.
3. Wu E, Judd RM, Vargas JD, et al. Visualisation of presence, location, and transmural extent of healed Q-wave and non-Q-wave myocardial infarction. Lancet 2001;357:21–28.
4. Klein MA, Collier BD, Hellman RS, et al. Detection of chronic coronary artery disease: value of pharmacologically stressed, dynamically enhanced turbo fast low angle shot MR images. AJR Am J Roentgenol 1993;161:39–542.
5. Penzkofer H, Wintersperger BJ, Knez A, et al. Assessment of myocardial perfusion using multisection first-pass MRI and color-coded parameter maps: a comparison to 99mTcSesta MIBI SPECT and systolic myocardial wall thickening analysis. Magn Reson Imaging 1999;17:161–170.
6. Wilke N, Jerosch-Herold M, Wang Y, et al. Myocardial perfusion reserve: assessment with multisection, quantitative, first-pass MR imaging. Radiology 1997;204:373–384.
7. Jerosch-Herold M, Wilke N, Stillman AE. Magnetic resonance quantification of myocardial perfusion reserve with a Fermi function model for constrained deconvolution. Med Phys 1998;25:73–84.
8. Edelman RR, Li W. Contrast-enhanced echo-planar MR imaging of myocardial perfusion: preliminary study in humans. Radiology 1994;190:771–777.
9. Panting JR, Gatehouse PD, Yang GZ, et al. Echo-planar magnetic resonance myocardial perfusion imaging: parametric analysis and comparison with thallium SPECT. J Magn Reson Imaging 2001;13:192–200.
10. Ibrahim T, Nekolla SG, Schreiber K, et al. Assessment of coronary flow reserve: comparison between contrast-enhanced magnetic resonance imaging and positron emission tomography. J Am Coll Cardiol 2002;39:864–870.
11. Ding S, Wolff SD, Epstein FH. Improved coverage in dynamic contrast-enhanced cardiac MRI using interleaved gradient echo EPI. Magn Reson Med 1998;39:514–519.
12. Fenchel M, Helber U, Simonetti OP, et al. Multislice first-pass myocardial perfusion imaging: comparison of saturation recovery (SR)-true FISP-two-dimensional (2D) and SR-TurboFLASH-2D pulse sequences. J Magn Reson Imaging 2004;19:555–563.
13. Schreiber WG, Schmitt M, Kalden P, et al. Dynamic contrast-enhanced myocardial perfusion imaging using saturation-prepared TrueFISP. J Magn Reson Imaging 2002;16:641–652.
14. Hunold P, Maderwald S, Eggebrecht H, et al. Steady state free precession sequences in myocardial first-pass perfusion MR imaging: comparison with TurboGRE imaging. Eur Radiol 2004;14:409–416.
15. Kostler H, Sandstede JJW, Lipke C, et al. Auto-SENSE perfusion imaging of the whole heart. J Magn Reson Imaging 2003;18:702–708.
16. Kellman P, Derbyshire JA, Ageyman KO, et al. Extended coverage first pass perfusion using sliceinterleaved TSENSE. Magn Reson Med 2004;51:200–204.
17. Pruessmann KP, Weiger M, Scheidegger MB, et al. SENSE: sensitivity encoding for fast MRI. Magn Reson Med 1999;42:952–962.
18. Kellman P, Epstein FH, McVeigh ER. Adaptive sensitivity encoding incorporating temporal filtering (TSENSE). Magn Reson Med 2001;45:846–852.
19. Griswold MA, Jakob PM, Heidemann RM, et al. Generalized autocalibrating partially parallel acquisitions (GRAPPA). Magn Reson Med 2002;47:1202–1210.

20. Hunold P, Maderwald S, Ladd ME, et al. Parallel acquisition techniques in cardiac cine magnetic resonance imaging using TrueFISP sequences: comparison of image quality and artifacts. J Magn Reson Imaging 2004;20:06–511.
21. Ingkanisorn WP, Rhoads KL, Syed MA, et al. Fat suppression improves image quality and diagnostic accuracy of EPI first pass perfusion. In: Proc 12th Scientific Meeting ISMRM 2004;312.
22. Deshpande VS, Shea SM, Chung YC, McCarthy RM, Finn JP, Li D. Breath-hold threedimensional true-FISP imaging of coronary arteries using asymmetric sampling. J Magn Reson Imaging 2002;15: 473–478.
23. Deshpande VS, Chung YC, Zhang Q, Shea SM, Li D. Reduction of transient signal oscillations in true-FISP using a linear flip angle series magnetization preparation. Magn Reson Med 2003;49:151–157.
24. Bernstein MA, King KF, Zhou XJ. Handbook of MRI pulse sequences. Elsevier Academic Press, Burlington, MA; 2004:579-580.
25. Bernstein MA, King KF, Zhou XJ. Handbook of MRI pulse sequences. Elsevier Academic Press, Burlington, MA; 2004:585.
26. Kellman P, McVeigh ER. Image reconstruction in SNR units: a general method for SNR measurement. Magn Reson Med 2005;54: 1439–1447.
27. De Wilde JP, Lunt JA, Straughan K. Information in magnetic resonance images: evaluation of signal, noise and contrast. Med Biol Eng Comput 1997;35:259–265.
28. Haacke M, Brown R, Thompson M, et al. Magnetic resonance imaging: physical principles and sequence design. New York: Wiley-Liss; 1999.
29. Elkington AG, Gatehouse PD, Cannell TM, et al. Comparison of hybrid echo-planar imaging and GRE myocardial perfusion cardiovascular MR imaging. Radiology 2005;235:237–243.
30. Cerqueira MD, Weissman NJ, Dilsizian V, et al. Standardized myocardial segmentation and nomenclature for tomographic imaging of the heart: a statement for healthcare professionals from the Cardiac Imaging Committee of the Council on Clinical Cardiology of the American Heart Association. Circulation 2002;105:539–542.
31. Storey P, Chen Q, Li W, et al. Band artifact due to bulk motion. Magn Reson Med 2002;48:1028–1036.
32. Di Bella EVR, Parker DL, Sinusas AJ. On the dark rim artifact on dynamic contrast-enhanced MRI myocardial perfusion studies. Magn Reson Med 2005;54:1295–1299.
33. Wang Y, Moin K, Akinboboye O, et al. Myocardial first pass perfusion: steady-state free precession versus spoiled gradient echo and segmented echo planar imaging. Magn Reson Med 2005;54:1123–1129.
34. Gebker R, Paetsch I, Neuss M, et al. Determinants of myocardial response in CMR perfusion imaging using Gd-BOPTA (Mulithance). J Cardiovasc Magn Reson 2005;7:565–572.
35. Muhling OM, Dickson ME, Zenovich A, et al. Quantitative magnetic resonance first-pass perfusion analysis: inter- and intraobserver agreement. J Cardiovasc Magn Reson 2001;3:247–256.